

Global Linear and Nonlinear Gyrokinetic Simulations of Tearing Modes

**T. Jitsuk¹, A. Di Siena², M.J. Pueschel³, P.W. Terry¹,
F. Widmer⁴, E. Poli², and J.S. Sarff¹**

¹Department of Physics, University of Wisconsin-Madison, WI 53706, USA

²Max-Planck-Institut für Plasmaphysik, D-85748 Garching, Germany

³Dutch Institute for Fundamental Energy Research, 5612 AJ Eindhoven,
The Netherlands

⁴International Research Collaboration Center, National Institutes of Natural
Sciences, Tokyo 181-8588, Japan

E-mail: jitsuk@wisc.edu

1 September 2023

Abstract. To better understand the interaction of global tearing modes and microturbulence in the Madison Symmetric Torus (MST) reversed-field pinch (RFP), the global gyrokinetic code GENE is modified to describe tearing mode instability via a shifted Maxwellian distribution consistent with experimental equilibria. The implementation of the shifted Maxwellian is tested and benchmarked by comparisons with different codes and models. Good agreement is obtained in code-code and code-theory comparisons. Linear stability of tearing modes of a non-reversed MST discharge is studied. A collisionality scan is performed to the lowest order unstable modes ($n = 5$, $n = 6$) and shown to behave along with theoretical scaling. The nonlinear evolution is simulated, and saturation is found to arise from mode coupling and transfer of energy from the most unstable tearing mode to small-scale stable modes mediated by the $m = 2$ tearing mode. The work described herein lays the foundation for nonlinear simulation and analysis of the interaction of tearing modes and gyroradius-scale instabilities in the RFP.

1. Introduction

Tearing modes are a familiar type of fluctuation in toroidally-confined plasmas and can significantly influence the stability and performance of fusion devices. They produce magnetic islands, are associated with cyclical oscillations like sawteeth, drive disruptive events, and can lead to turbulence with its significant plasma transport and energy losses [1, 2]. When tearing modes excite a turbulent cascade, fluctuation energy reaches small scales where it can impact microscale instabilities and fluctuations. Extensive research has been dedicated to understanding the linear and nonlinear physics of tearing modes, and in developing effective strategies to mitigate their detrimental effects.

One particular toroidal device where tearing modes are active and play a fundamental role in plasma dynamics is the reversed-field pinch (RFP) [3, 4, 5, 6, 7, 8, 9]. Tearing modes in RFPs are global, system-scale modes driven by the current profile across its radial domain. These modes grow to finite amplitude and exhibit nonlinear couplings with each other and with small-scale fluctuations. Experimental measurements and nonlinear magnetohydrodynamic (MHD) computations have provided detailed analyses, revealing that the coupling between tearing modes of different poloidal and toroidal mode numbers m and n leads to the conversion of poloidal magnetic flux in the plasma core region to toroidal magnetic flux near the reversal surface. This results in a self-generated toroidal flux, commonly referred to as the dynamo effect [3, 10]. Moreover, interactions among multiple tearing modes resonant at different radii enhance energy and momentum transport [11, 12]. When the activity of tearing modes is reduced through control of the plasma current profile in pulsed-poloidal-current-drive (PPCD) experiments, plasma confinement improves, characterized by increasing plasma beta and electron temperature, as well as reduced electron heat diffusivity [8]. RFPs can furthermore exhibit a plasma state called quasi-single-helicity (QSH) where the lowest resonant mode at the innermost radii singly dominates the tearing-mode spectrum, leaving other higher resonant modes at larger radii insignificant. The regime is equivalent to having multiple tearing modes suppressed which limits nonlinear interactions, leading to less magnetic stochasticity, increased plasma current, and hence enhanced confinement [13, 14, 15].

Nonlinear interactions involving tearing modes occur not only between global-scale modes but also across an extended range of scales, as directly observed and inferred in a number of experiments [16, 17, 18]. As tearing modes cascade to small scales, they continue to interact with MHD fluctuations. They can also interact with drift-wave-type micro-instabilities and turbulence. Such interactions, which involve not just different scales but different physics, are often described as multi-scale interactions. An example of a multi-scale interaction was demonstrated in a gyrokinetic simulation of density-gradient-driven trapped-electron-mode (∇n -TEM) turbulence in the RFP with a representation of tearing mode activity in terms of a constant-in-time magnetic-field perturbation modeling residual tearing fluctuations. The simulations showed that the magnetic fluctuation suppressed the zonal flows generated nonlinearly in TEM turbulence, resulting in an increase of the electrostatic heat flux [19].

Similar effects stemming from large-scale magnetic perturbations on zonal-flow-mediated microturbulence have also been observed in the tokamak. Resonant magnetic perturbations (RMPs), which are externally applied to plasmas for the suppression of edge-localized modes [20], were found in DIII-D experiments to increase transport levels and lower energy confinement [21]. Local gyrokinetic simulations using a *ad-hoc* radial magnetic perturbation similar to that of RFP modeling were carried out for a DIII-D L-mode scenario. The simulations indicate that incremental increases in turbulent fluctuations are related to the reduction of zonal-flow levels by this perturbation [22]. Similarly, the interaction between microtearing and electron-scale

turbulence is partly governed by zonal flows and can be regulated via the addition of RMPs [23]. Thus, the physical mechanism at play is largely the same as that in the RFP. This modeling approach is most appropriate for external perturbations like the RMP. It is an approximation for the effect of internal magnetic perturbations from collective modes, both because collective modes have their internally consistent linear and nonlinear structure and because external perturbations cannot capture any possible back-reaction of the microturbulence on the collective mode. This motivates the present, more realistic and accurate approach.

Although extensive investigations have been conducted to examine self-interacting tearing modes within the RFP, interactions simultaneously involving micro- and macro-scale fluctuations have received comparatively limited attention and are therefore less understood. The limited progress on multi-scale interactions to date is due, at least in part, to the fact that the self-consistent coupling of two distinct scales is difficult to treat computationally. While studies of single-scale tearing modes and nonlinear couplings of different helicities can be performed solely within MHD models, coupling with microinstabilities requires models that can capture gyroradius-scale drift-wave physics. One class of drift-wave-capable models is gyrokinetics [24], which generally provides a comprehensive representation of micro-scale instability physics. Attempts have also been directed toward employing the gyrokinetic model to study global MHD modes. One of the prior studies developed the particle-in-cell gyrokinetic toroidal code (GTC), coupling fluid electron description into gyrokinetic ions, reproduced resistive tearing modes [25] and collisionless tearing modes [26], and verified by exhibiting correct eigenmode structures and growth-rate scaling in comparison with MHD computations. A self-consistent modeling of tearing modes was further developed in the continuous δf code GKW, specifically in studying the stability of linear tearing modes in three-dimensional toroidal geometry [27], and later in the study of the seed-island generation and nonlinear interaction of tearing mode and electromagnetic turbulence [1, 28].

As already stated, previous gyrokinetic studies of multi-scale interactions in RFP plasmas imposed a constant-in-time external A_{\parallel} as a simple model for a residual tearing fluctuation [19, 29]. However, tearing-scale instabilities in experiments are internally consistent collective modes driven by a radial gradient in the background current parallel to the mean magnetic field. To better model this situation, a self-consistent description is needed. To this end, Ref. [30] implemented a current-gradient drive as part of the fluctuating distribution function. The implementation, restricted to slab geometry, allowed for a sinusoidal current profile with adjustable magnitude and phase, which are able to drive a (slab) tearing mode. Several aspects of this approach impose limitations: local slab simulations do not allow for a realistic equilibrium, and linear solutions of the gyrokinetic model equations result in slab-specific intermediate-scale modes. As these are not present in the experiment, they interfere with the study of experimentally relevant multi-scale interactions.

To more realistically model tearing modes, a shifted Maxwellian equilibrium distribution is implemented in the global version of the gyrokinetic code GENE

[31, 32, 33, 34, 35], consistent with a specified safety factor profile. Details related to the implementation of the shifted Maxwellian distribution are presented in this work, including the equilibrium distribution with shifted velocity, its effect on the perturbed distribution and the instability driving terms, and its modification of velocity moments that enter into the calculation of the self-consistent fields. The implementation is then benchmarked against several plasma models, including a reduced fluid model and gyrokinetic codes based on both continuum δf and particle-in-cell full- f approaches. Of particular note is benchmarking with the ORB5 code [36], which is also modified to incorporate a shifted Maxwellian equilibrium distribution for current-gradient-driven modes. In preparation for multi-scale simulations, linear tearing modes in a non-reversed RFP discharge are obtained. Linear initial-value calculations for the fastest-growing mode show that the lowest resonant mode is dominant. At large k_y the fluctuations become electrostatic and are identified as ∇n -TEMs [37]. The nonlinear evolution of the RFP tearing mode is obtained and studied in detail for the first time in gyrokinetics. These studies provide the basis for carrying out multi-scale interactions of tearing modes with gyroradius-scale turbulence in future work.

The remainder of the paper is organized as follows. Details of the numerical approach as well as the gyrokinetic treatment of the current gradient and its implementation are discussed in Sec. 2. Numerical benchmarking against a variety of published results is elaborated in Sec. 3. Linear and nonlinear tearing mode evolution in the RFP system are studied in Sec. 4, and a summary and discussion are provided in Sec. 5.

2. Current-Gradient Implementation

The gyrokinetic framework [24] allows for the evaluation of microinstability physics as well as nonlinear interactions between fluctuations across a range of scales. Here, the global version of the gyrokinetic turbulence code GENE [31, 32, 35], is employed, which has been used with non-Maxwellian background distributions [33, 38]. GENE solves a Vlasov-Maxwell system of equations with a δf approach, in which the total distribution f is split into the static background distribution F_0 and the perturbed distribution δf , such that $f = F_0 + \delta f$, with self-consistent field equations. Writing f in terms of the modified distribution g , where $g_j = f_j - q_j/(cm_j)\partial_{v_\parallel}F_{0j}\bar{A}_\parallel$ with j the species index, the form of the gyrokinetic Vlasov equation for each plasma species j is represented by

$$\frac{\partial g_j}{\partial t} = \mathcal{L}[g_j] + \mathcal{N}[g_j]. \quad (1)$$

In this equation, \mathcal{L} is the linear operator, containing among other terms the instability drive due to profile gradients for small-scale drift-wave instabilities, and \mathcal{N} is the electromagnetic version of the $\mathbf{E} \times \mathbf{B}$ nonlinearity that couples different interacting modes. The modifications entailed in the present work will add to \mathcal{L} the energy source for large-scale current-driven modes.

2.1. Shifted Maxwellian Background Distribution

Global tearing instabilities are driven by the current gradient in the plasma. However, the conventional GENE code assumes a Maxwellian as the background distribution, resulting in zero parallel current density under the first velocity moment. While more recent versions of the code offer non-Maxwellian distributions, e.g., the bi-Maxwellian [33], they still yield a zero current density. To accurately model current-gradient-driven instabilities and replicate experimental observations, a shifted Maxwellian (SM) background distribution is employed to capture the realistic driving mechanism. Specifically, the background distribution for particle species j is expressed as

$$F_{\text{SM},j} = \frac{n_{0j}(x) m_j^{3/2}}{(2\pi T_{0j}(x))^{3/2}} \exp \left[-\frac{(v_{\parallel} - v_{\parallel 0,j}(x))^2}{2T_{0j}(x)/m_j} - \frac{\mu B_0(x)}{T_{0j}(x)} \right]. \quad (2)$$

In Eq. (2), $n_{0j}(x)$ and $T_{0j}(x)$ are the equilibrium density and temperature, m_j is the particle mass, $B_0(x)$ is the equilibrium magnetic field, and $v_{\parallel 0,j}(x)$ is the velocity shift in the parallel direction, normalized to the thermal velocity $v_{\text{Th},j} = [2T_{0j}(x_0)/m_j]^{1/2}$ at the reference location x_0 of the simulation domain. Although later not explicitly written, this parallel shift is x -dependent. Various terms in the linear operator of the gyrokinetic equation are modified according to the change in the background distribution function. One important term is the radial derivative of the background distribution, contributing to the gradient drive term,

$$\begin{aligned} \nabla_x F_{\text{SM},j} = & -F_{\text{SM},j} \left\{ \omega_{Tj} \left[\frac{(v_{\parallel} - v_{\parallel 0,j})^2 + \mu B_0}{2T_{0j}/m_j} - \frac{3}{2} \right] + \omega_{nj} \right. \\ & \left. - \frac{2(v_{\parallel} - v_{\parallel 0,j}) \nabla_x v_{\parallel 0,j} - (v_{\parallel 0,j}/v_{\parallel}) \mu \nabla_x B_0}{2T_{0j}/m_j} \right\}. \end{aligned} \quad (3)$$

Here, $\omega_{Tj} \equiv -L_{\text{ref}} \nabla_x \ln T_{0j}$ and $\omega_{nj} \equiv -L_{\text{ref}} \nabla_x \ln n_{0j}$ are the temperature and density gradient scale lengths, respectively. These gradients are the energy source for well-known, particularly electrostatic, micro-instabilities. The parallel velocity and the magnetic moment are denoted, respectively, v_{\parallel} and μ . We note that L_{ref} is a reference length scale, typically set to be the major radius R_0 for global calculations. The last term, involving the gradient of the shifted velocity, introduces the new driving force into the system, i.e., the current-gradient drive, as $\nabla v_{\parallel 0} \propto \nabla J_{\parallel 0}$.

2.2. Modifications to the Field Equations

The perturbed electrostatic potential $\phi(\mathbf{x})$ can be evaluated using the Poisson equation

$$\nabla_{\perp}^2 \phi_1(\mathbf{x}) = -4\pi \sum_j q_j n_{1,j}(\mathbf{x}) = -4\pi \sum_j q_j M_{00,j}(\mathbf{x}). \quad (4)$$

Gaussian units are used, and all quantities are later normalized according to the GENE convention, with further details provided in Ref. [34]. The density $n_{1,j}(\mathbf{x})$ is expressed in terms of the zeroth moment $M_{00,j}(\mathbf{x})$ of the distribution with respect to v_{\parallel} and μ . In gyrokinetics, the particle coordinates \mathbf{x} can be decomposed into the gyration center \mathbf{X}

and the radial displacement \mathbf{r} from the gyration center in the perpendicular plane, such that $\mathbf{x} = \mathbf{X} + \mathbf{r}$. By employing the appropriate moments described in Refs. [33, 34, 38], and neglecting parallel magnetic field fluctuations, the Poisson equation can be written as

$$\begin{aligned} \nabla_{\perp}^2 \phi_1(\mathbf{x}) = & -\frac{8\pi^2 q B_0}{m} \int \int \left\{ \langle f_1(\mathbf{x} - \mathbf{r}) \rangle \right. \\ & + \left[\frac{\Omega}{B_0} \frac{\partial F_{\text{SM}}}{\partial v_{\parallel}} - \frac{qv_{\parallel}}{cB_0} \frac{\partial F_{\text{SM}}}{\partial \mu} \right] (A_{1,\parallel}(\mathbf{x}) - \langle \bar{A}_{1,\parallel}(\mathbf{x} - \mathbf{r}) \rangle) \\ & \left. + \left[\frac{q}{B_0} (\phi_1(\mathbf{x}) - \langle \bar{\phi}_1(\mathbf{x} - \mathbf{r}) \rangle) \right] \frac{\partial F_{\text{SM}}}{\partial \mu} \right\} dv_{\parallel} d\mu. \end{aligned} \quad (5)$$

$\langle \dots \rangle$ and overbars represent the gyroaverages defined as $\bar{\phi}_1 = \langle \phi_1(\mathbf{x}) \rangle = \mathcal{G}[\phi_1(\mathbf{x})] = \int \phi_1(\mathbf{X} + \mathbf{r}(\theta)) d\theta / 2\pi$, with the gyroradius vector $\mathbf{r}(\theta)$ orthogonal to the magnetic field, and gyroangle θ , $\langle \bar{A}_{1,\parallel}(\mathbf{x} - \mathbf{r}) \rangle$ is the double gyroaverage of the vector field $A_{1,\parallel}$ defined as $\int d\theta \int d\mathbf{X} \delta(\mathbf{X} + \mathbf{r}(\theta) - \mathbf{x}) \int d\theta' A_{\parallel}(\mathbf{X} + \mathbf{r}(\theta')) d\theta' / 4\pi^2$, which in the global version is written as $\mathcal{G}^{\dagger} A_{1,\parallel}(\mathbf{x} - \mathbf{r}) \mathcal{G}$, as seen in some expressions later in the paper. This double gyroaverage arises from integration of the velocity moment $M_{00,j}$, which contains another gyroaverage of the perturbed distribution function [34]. The same applies to the electrostatic potential terms. Under the Coulomb gauge and in the absence of an equilibrium electric field, the parallel vector potential is calculated from Ampère's law and given by

$$\nabla_{\perp}^2 A_{1,\parallel}(\mathbf{x}) = -\frac{4\pi}{c} \sum_j q_j v_{\parallel 0,j}(\mathbf{x}) n_{1,j}(\mathbf{x}) = -\frac{4\pi}{c} \sum_j q_j M_{10,j}(\mathbf{x}). \quad (6)$$

This expression can be similarly written in terms of the shifted Maxwellian, yielding

$$\begin{aligned} \nabla_{\perp}^2 A_{1,\parallel}(\mathbf{x}) = & -\frac{8\pi^2 q}{mc} \int \int \left\{ \langle f_1(\mathbf{x} - \mathbf{r}) \rangle \right. \\ & + \left[\frac{\Omega}{\partial v_{\parallel}} \frac{\partial F_{\text{SM}}}{\partial v_{\parallel}} - \frac{qv_{\parallel}}{c} \frac{\partial F_{\text{SM}}}{\partial \mu} \right] (A_{1,\parallel}(\mathbf{x}) - \langle \bar{A}_{1,\parallel}(\mathbf{x} - \mathbf{r}) \rangle) \\ & \left. + q [\phi_1(\mathbf{x}) - \langle \bar{\phi}_1(\mathbf{x} - \mathbf{r}) \rangle] \frac{\partial F_{\text{SM}}}{\partial \mu} \right\} dv_{\parallel} d\mu. \end{aligned} \quad (7)$$

Combining Poisson's equation and Ampère's law results in coupled field equations, which can be written in matrix form as

$$\begin{bmatrix} C_1 & C_2 \\ C_3 & C_4 \end{bmatrix} \begin{bmatrix} \phi_1 \\ A_{1,\parallel} \end{bmatrix} = \begin{bmatrix} N_{00} \\ N_{10} \end{bmatrix} \quad (8)$$

The potentials are solved by inverting the matrix $[C_i]$, yielding

$$\begin{bmatrix} \phi_1 \\ A_{1,\parallel} \end{bmatrix} = \frac{1}{C_1 C_3 - C_2 C_4} \begin{bmatrix} C_4 & -C_2 \\ -C_3 & C_1 \end{bmatrix} \begin{bmatrix} N_{00} \\ N_{10} \end{bmatrix} \quad (9)$$

where

$$\begin{aligned} C_1 &= \frac{\pi q^2 n_0}{T_0} \int \int \left[\frac{B_0 F_{\text{SM}}}{T_0(x)} \hat{\mathbf{1}} - \mathcal{G}^{\dagger} \frac{B_0 F_{\text{SM}}}{T_0(x)} \mathcal{G} \right] dv_{\parallel} d\mu - \nabla_{\perp}^2 \lambda_{\text{De}}^2, \\ C_2 &= \frac{2\pi q^2 n_0}{mv_{\text{Th}}} \int \int \left[-\frac{B_0 v_{\parallel 0} F_{\text{SM}}}{T_0(x)} \hat{\mathbf{1}} + \mathcal{G}^{\dagger} v_{\parallel} \frac{B_0 F_{\text{SM}}}{T_0(x)} \mathcal{G} \right] dv_{\parallel} d\mu, \end{aligned}$$

$$\begin{aligned}
C_3 &= \frac{\pi q^2 n_0 \beta_{\text{ref}}}{mv_{\text{Th}}} \int \int v_{\parallel} \left[\frac{B_0 F_{\text{SM}}}{T_0(x)} \hat{\mathbf{1}} - \mathcal{G}^\dagger \frac{B_0 F_{\text{SM}}}{T_0(x)} \mathcal{G} \right] dv_{\parallel} d\mu, \\
C_4 &= -\nabla_{\perp}^2 - \frac{\pi q^2 n_0 \beta_{\text{ref}}}{m} \int \int \left[\frac{B_0 v_{\parallel} v_{\parallel 0} F_{\text{SM}}}{T_0(x)} \hat{\mathbf{1}} - \mathcal{G}^\dagger v_{\parallel}^2 \frac{B_0 F_{\text{SM}}}{T_0(x)} \mathcal{G} \right] dv_{\parallel} d\mu, \\
N_{00} &= \pi q n_0 B_0 \int \int \mathcal{G}(g_1(\mathbf{x})) dv_{\parallel} d\mu, \text{ and} \\
N_{10} &= \pi q n_0 \beta_{\text{ref}} \frac{B_0 v_{\text{Th}}}{2} \int \int v_{\parallel} \mathcal{G}(g_1(\mathbf{x})) dv_{\parallel} d\mu.
\end{aligned}$$

The diagonal elements of the gyroaverage matrix are written as $\hat{\mathbf{1}}$, while $T_0 = T_0(x_0)$ and $n_0 = n_0(x_0)$ are the temperature and density at the reference position x_0 . The modified field equations couple the electrostatic and electromagnetic potentials, in contrast to the conventional equations derived from the Maxwellian distribution function, where the two are decoupled. This coupling allows for the consideration of the influence of a magnetic perturbation on the electrostatic field, as expected in self-consistent calculations of tearing modes [39, 40]. The re-derivation of velocity moments related to observable quantities, such as electromagnetic heat and particle fluxes, is also incorporated into the code to account for the modified transport caused by tearing instabilities.

2.3. Parallel Current Profile

The shifted Maxwellian distribution function requires as input the velocity shift profile $v_{\parallel 0}(x)$, which can be evaluated from the equilibrium parallel current density based on the equation of the first velocity moment of the shifted Maxwellian

$$J_{\parallel 0}(x) = \sum_j q_j v_{\parallel 0,j}(x) n_{0j}(x) = \sum_j q_j \int v_{\parallel,j} F_{\text{SM},j} d^3 \mathbf{v}. \quad (10)$$

In the common scenario of a two-component-plasma current, ions and electrons tend to flow in opposite directions. Taking $|q_i| = e$, invoking the quasi-neutrality condition $n_{0e} = n_{0i} = n_0$, and assuming the flow velocities are on the order of the species' thermal velocities, with normalization $v_{\parallel 0,j} = \hat{v}_{\parallel 0,j} v_{\text{Th},j}$, where $\hat{v}_{\parallel 0,j}$ a dimensionless quantity, the current may be written as

$$J_{\parallel 0}(x) = J_{\parallel 0,i}(x) + J_{\parallel 0,e}(x) = e n_0(x) \hat{v}_{\parallel 0}(x) v_{\text{Th},e} \left[1 + \sqrt{\frac{T_{0e}}{T_{0i}} \frac{m_i}{m_e}} \right], \quad (11)$$

and thus the velocity shift reads

$$\hat{v}_{\parallel 0}(x) = \frac{J_{\parallel 0}(x)}{e n_0(x) v_{\text{Th},e}} \left[1 + \sqrt{\frac{T_{0e}}{T_{0i}} \frac{m_i}{m_e}} \right]^{-1}. \quad (12)$$

The current can also be extracted from the equilibrium profile of the safety factor q , as the q -profile contains information about the toroidal and poloidal magnetic fields. To enable benchmarks for established tearing mode behavior in tokamak geometry, we develop expressions relating q to the current that is appropriate for a large-aspect-ratio tokamak. Later, when the RFP is considered, we will directly use experimentally

relevant current profiles generated from the equilibrium solver MSTfit. For a large-aspect-ratio circular cross-section, the q -profile can be written in terms of the cylindrical approximation as

$$q(r) = \frac{r}{R_0} \frac{B_\varphi(r)}{B_\theta(r)}, \quad (13)$$

where $B_\varphi(r)$ and $B_\theta(r)$ are toroidal and poloidal magnetic fields, respectively, and r denotes the radial coordinate, which from this point can be used interchangeably with x . Starting with Ampère's law $(4\pi/c)\mathbf{J} = \nabla \times \mathbf{B}$, the cylindrical approximation with $B_\theta \ll B_\varphi \sim B_0$ yields a parallel current density given by

$$J_{\parallel 0}(r) \approx \frac{c}{4\pi} \left[\frac{1}{r} \frac{\partial(rB_\theta)}{\partial r} \right] = \frac{cB_0}{4\pi R_0} \frac{\partial}{r\partial r} \left[\frac{r^2}{q(r)} \right]. \quad (14)$$

The prefactor $cB_0/(4\pi R_0)$ is equivalent to the current density $J_{\parallel 0}$ at the axis. Equating this expression to Eq. (12), the velocity shift can be written as

$$\hat{v}_{\parallel 0}(r) = \frac{cB_0/(4\pi R_0)}{n_0(r)e v_{\text{Th,e}}} \left[1 + \sqrt{\frac{T_{0e}}{T_{0i}} \frac{m_i}{m_e}} \right]^{-1} \left[\frac{\partial}{r\partial r} \left(\frac{r^2}{q} \right) \right]. \quad (15)$$

In terms of normalized parameters, the dimensionless velocity shift is equivalently given by

$$\hat{v}_{\parallel 0}(r) = \frac{\sqrt{2}\varepsilon_a \rho_i^*}{\hat{n}_0(r)\beta_e} \left[1 + \sqrt{\frac{T_{0e}}{T_{0i}} \frac{m_i}{m_e}} \right]^{-1} \left[\frac{\partial}{r\partial r} \left(\frac{r^2}{q(r)} \right) \right], \quad (16)$$

where $\beta_e = 8\pi n_{0e} T_{0e} / B_0^2$, $\rho_i^* = \rho_i/a$, $\varepsilon_a = a/R_0$, and $\hat{n}_0(r) = n_0(r)/n_0(r_0)$, with r_0 the reference position in the simulation domain. Also note that the electron skin depth δ_e can be written directly as

$$\frac{\delta_e}{a} = \sqrt{\frac{m_e}{m_i} \frac{T_{0e}}{T_{0i}}} \frac{\rho_i^*}{\sqrt{\beta_e/2}}, \quad (17)$$

and that this form relates to the strength of velocity shift as shown in Eq. (16). The electron skin depth is related to the singular layer width, allowing the determination of tearing mode behavior and stability regimes [40, 41].

3. Benchmarking of the Current-Gradient Drive

The implementation of a shifted Maxwellian based on a velocity shift in the Vlasov-Maxwellian system of equations represents a significant modification to GENE, enabling self-consistent global simulations of current-driven instabilities. Before deploying this upgraded code to study linear tearing instability, nonlinear tearing evolution, and later multi-scale interactions in the RFP, it is important to test the fidelity of the implementation against different computational models. The analytic forms of the equilibrium profiles and other input parameters, for which tearing modes are unstable, are listed in Table 1.

| Equilibrium | ORB5 | GKW Hornsby <i>et al.</i> [27, 28] | Two-Fluid Ishizawa <i>et al.</i> [42] |
|--|--------------------------|--|--|
| $q(x_a)$ | $\sum_{i=0}^8 c_i x_a^i$ | $3.5x_a^2[1 - (1 - x_a^2)^2]^{-1}$ $(R/L_T) \int [\tanh(100x_a - 5) - \tanh(100x_a - 105)]/2dx_a$ | $1.7(1 + 29.65x_a^8)^{1/4}$ $0.8 - 0.2 \tanh(5x_a - 3.5)$ |
| $T_i = T_e = T_{eq}(x_a)$ | 1 | $(R/L_n) \int [\tanh(100x_a - 5) - \tanh(100x_a - 105)]/2dx_a$ | $0.8 + 0.2 \exp(-4x_a^2)$ |
| $n_i = n_e = n_{eq}(x_a)$ | 1 | 0.1% | 1% |
| $\beta_e = 8\pi n_e T_e / B_0^2$ | 0.2% | 0.0118 | 0.0125 |
| $\rho_i^* = \rho_i/a$ | 0.01 | 0.3 | 0.25 |
| $\varepsilon_a = a/R_0$ | 0.1 | 0.000544 | 0.000544 |
| m_e/m_i | 0.005 | 0.00112 | 0.03187 |
| ν_c | 0 | | |
| domain $[x_a^{\min}, x_a^{\max}]$ | [0.01, 0.99] | [0.1, 1] | [0.01, 0.99] |
| buffers [left, right] | [0.1a, 0.1a] | [0.05a, 0.05a] | [0.05a, 0.05a] |
| hyp _x , hyp _z , hyp _v | 0.2, -1, 0.2 | 0.1, -1, 0.2 | 0.05, -1, 0.1 |

Table 1. Analytic forms of equilibrium profiles and parameters used for benchmarks in this work. Note that $x_a = x/a$ is the normalized radius. q , T_{eq} , n_{eq} , β_e , ρ_i , a , R_0 , m_e , and m_i are safety factor, equilibrium temperature, equilibrium density, plasma beta, ion gyroradius, device minor radius, major radius, electron mass, and ion mass, respectively. Note for the safety factor profile in the ORB5 case, $q(x_a) = \sum_{i=0}^8 c_i x_a^i$, with coefficients $c_i = (1.4950, -0.0052, 0.7969, -1.2433, 6.0576, -14.4208, 20.4868, -15.1526, 4.8045)$. The bottom half panel displays the boundary constraints [43] and hyperdiffusivities [44] set in GENE. x_a^{\min} and x_a^{\max} are the left and the right ends of the simulation domain, respectively, buffer refers to the size of the left and right buffer zones, measured in minor radius, a , and hyp_i is the hyperdiffusivity applied to i direction.

3.1. Comparisons with ORB5

Linear global tearing modes simulated in the GENE code are compared with the results obtained from the gyrokinetic PIC code ORB5. Prior to this investigation, both codes have demonstrated successful benchmarking for scenarios involving global ion temperature gradient (ITG) and kinetic ballooning modes (KBMs) [32], geodesic acoustic modes (GAMs) [45], energetic-particle-driven GAMs (EGAMs) [38], and toroidal Alfvén eigenmodes (TAEs) [46]. Notably, a recent extension of the ORB5 code incorporates the current-gradient drive, similar to the capabilities of GENE presented here. Consequently, this benchmarking exercise presents the first simulations of linear tearing modes using the ORB5 code.

The equilibrium safety factor $q(x_a)$, where $x_a = x/a$ and a is a minor radius, for this test is an 8th-order polynomial which is unstable to an $m/n = 2/1$ tearing mode, where m and n are the poloidal and toroidal mode numbers, respectively. The polynomial coefficients c_i are given in Table 1, and the corresponding profiles are shown in Fig. 1, including the velocity shift profile calculated under the cylindrical approximation [see Eq. (16)]. The background temperature and density are assumed to be radially constant to avoid pressure-gradient-driven modes and diamagnetic effects. A small-inverse-aspect-ratio concentric circular geometry is used, making the cylindrical approximation justifiable and minimizing curvature effects. This makes comparison of the numerical growth rates with theoretical scalings of slab current sheets possible [40, 41]. For simplicity, the standard case sets collisionality ν_{ei} to zero, resulting in a

collisionless tearing mode (CTM). A list of other parameters is given in Table 1.

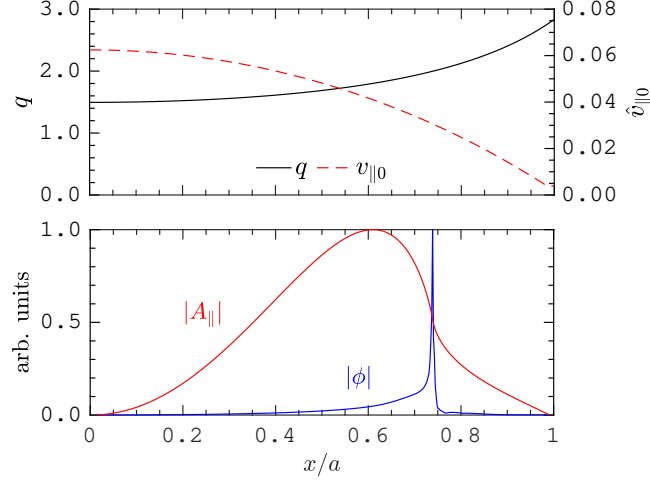


Figure 1. [Top] Profiles of the safety factor (black solid line, left axis) and the velocity shift (red dashed line, right axis) used for the benchmark with ORB5. [Bottom] The corresponding normalized radial eigenmode structures computed in GENE, for $n = 1$ corresponding to a tearing mode at $x/a \approx 0.74$, where $q = 2$

For $n = 1$, corresponding to $k_y \rho_s = 0.034$, GENE produces a tearing mode with growth rate $\gamma_{\text{GENE}} = 0.045 c_s / R_0 = 4.5 \times 10^{-5} \Omega_{ci}$, where $c_s = \sqrt{T_{0e}/m_i}$ is ion acoustic speed, and $\Omega_{ci} = (c_s / R_0) / (\varepsilon_a \rho_i^*)$ is the ion cyclotron frequency. ORB5 gives $\gamma_{\text{ORB5}} = 5.5 \times 10^{-5} \Omega_{ci}$, in good agreement with GENE. The growth rates are very small compared to the cyclotron frequency, and are roughly an order of magnitude slower than the growth of ion-scale instabilities, reflecting the characteristic time scale of tearing-mode fluctuations. The radial ϕ and A_{\parallel} eigenmode structures from GENE are shown in the bottom panel of Fig. 1 trace those of ORB5. Discontinuities across the rational surface $q = 2$ of ϕ and A_{\parallel} showing $\Delta' > 0$ are well-known indications of an unstable

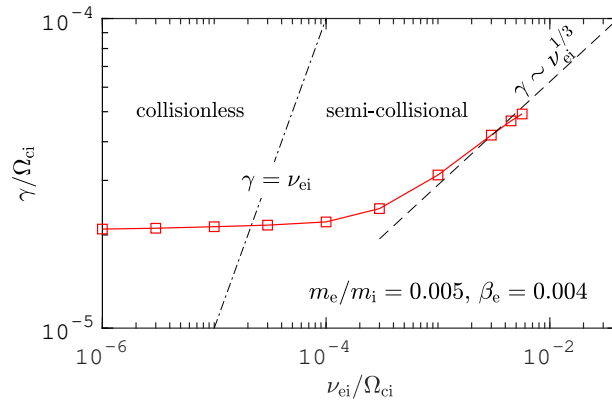


Figure 2. Tearing-mode growth rate as a function of electron-ion collision frequency, computed with GENE. Scaling consistent with theoretical prediction, is shown i.e, no dependence in the collisionless regime and $\gamma \propto \nu_{ei}^{1/3}$ in the semi-collisional regime.

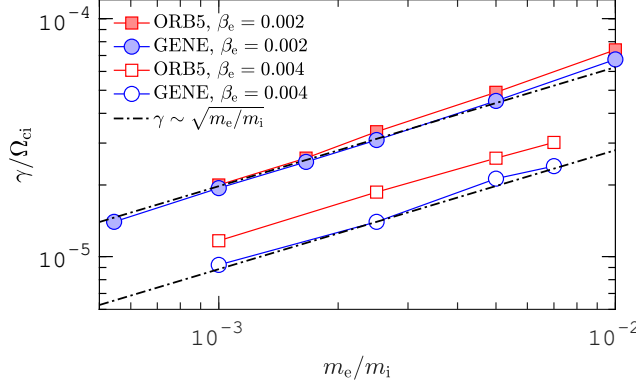


Figure 3. Mass ratio scan, simulations from GENE (blue circles) and ORB5 (red squares) at two different values of $\beta_e = \beta_e^{\text{GENE}} = 8\pi n_e T_e / B_0^2$. Note that $\beta_e^{\text{GENE}} = 2\beta_e^{\text{ORB5}}$. The theoretical growth rate scaling $\gamma \propto \sqrt{m_e/m_i}$ is shown as the black dashed line. Good agreement is observed between codes and theory.

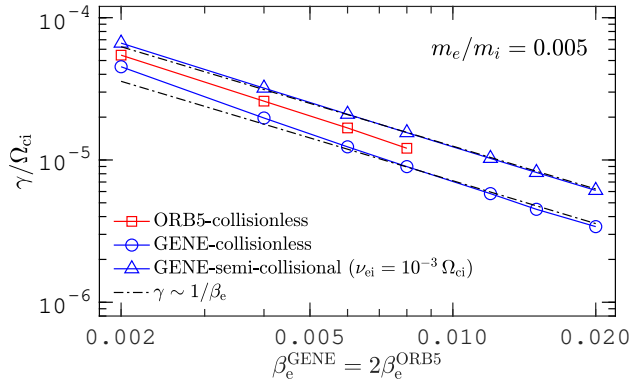


Figure 4. Collisionless β_e scans performed with GENE (blue circles) and ORB5 (red squares). The two codes agree with each other and with the theoretical scaling $\gamma \propto 1/\beta_e$. Blue triangles show GENE data in the semi-collisional regime where the same scaling is recovered.

tearing mode.

In MHD, tearing modes are destabilized by resistivity [27, 39, 40, 41]. Here, the collision frequency, which relates to resistivity in MHD, is varied, and the response of the tearing mode is recorded. Collisionality in GENE for this paper, except where stated otherwise, is modeled by a Landau collision operator to reduce the computational cost; other collision operators produce comparable growth rates but with higher computational expense. The normalized collision frequency used in GENE is defined as

$$\nu_{\text{coll}} = \frac{\pi \ln \Lambda e^4 n_{\text{ref}} L_{\text{ref}}}{2^{3/2} T_{\text{ref}}^2}, \quad (18)$$

where constituting quantities are given in Gaussian units. The simplified form can be written as $\nu_{\text{coll}} = 2.3031 \times 10^{-5} \ln \Lambda L_{\text{ref}} n_{\text{ref}} / T_{\text{ref}}^2$, where $\ln \Lambda$ is the Coulomb

logarithm which can be expressed as $24 - \ln(\sqrt{10^7 n_{\text{ref}}}/T_{\text{ref}})$, with the referenced value of background density n_{ref} in the units of 10^{19} m^{-3} and temperature T_{ref} in the units of keV, and L_{ref} is the referenced length in meters. The electron-ion collision frequency can be written in units of c_s/R_0 as

$$\nu_{\text{ei}} = 4Z^2 \sqrt{\frac{m_i}{m_e}} \frac{c_s}{R_0} \nu_{\text{coll}}, \quad (19)$$

with the ion charge number Z and sound speed $c_s = \sqrt{T_{0e}/m_i}$, and m_i and m_e are ion and electron mass, respectively. ν_{ei} , hence, has the same unit as growth rate. The growth rate of the tearing mode as a function of collisionality is plotted in Fig. 2. Two collisionalality regimes are evident, a collisionless and a semi-collisional regime. In the limit of collisionless tearing, growth rates approach a constant when $\nu_{\text{ei}} \ll \gamma$, while in the semi-collisional regime $\nu_{\text{ei}} \sim \gamma$, growth rates approach a scaling of $\gamma \propto \nu_{\text{ei}}^{1/3}$ [40, 41]. Simulations at higher collision frequencies were also attempted to see if the collisional regime could be reached; however, numerical instability prevented further study of this regime. This scaling behavior confirms that the instability reproduced by the modified GENE is indeed a tearing mode.

To assess the agreement between GENE and ORB5 across varying plasma parameters and to investigate the scaling behavior of tearing modes in accordance with theoretical predictions, systematic scans of mass ratios at different β_e are conducted using the initial setup, focusing on the standard collisionless case. Fig. 3 presents the tearing-mode growth rates at different mass ratios, compared with the corresponding computations from ORB5. Not only do the growth rates obtained from the two codes exhibit good agreement, but they also exhibit consistent scaling with the theoretical prediction $\gamma \propto \sqrt{m_e/m_i}$ [40]. Additionally, a β scan is performed and compared with the results from ORB5 as depicted in Fig. 4, which shows that growth rates follow each other and fall into correct theoretical scaling $\gamma \propto 1/\beta_e$ [40]. Also confirmed by this figure is the fact that GENE is capable of reproducing the expected β -scaling in the semi-collisional limit.

3.2. Comparison with GKW

Simulations of tearing modes are conducted to compare the results with published findings from another gyrokinetic code, GKW [47]. Similar to GENE, GKW is a global gyrokinetic code that uses a δf -approach capable of computing current-gradient-driven instabilities [3]. Previous studies employing GKW have examined the linear and nonlinear evolution of global-scale tearing modes in tokamak systems using a shifted-Maxwellian distribution function [1, 27, 28]. Detailed information regarding code implementation can be found in those publications, noting the distinction that the field equations are coupled in GENE but decoupled in GKW. This decoupling arises from a negligible magnitude of velocity shift $v_{\parallel 0} \ll 1$, resulting in the apparent insignificance of coefficients C_2 and C_3 in Eq. 2.2, rendering them dismissible. It breaks down when the shifted velocity becomes larger as $v_{\parallel 0} \sim 1$. This assumption retains its validity within

the scope of this benchmark, due to the smallness of velocity shift; notwithstanding, a notable gradient exists. The successful simulation of tearing-mode evolution in GKW establishes it as a suitable computational tool for comparison with GENE.

The present benchmark is based on the equilibrium and parameters utilized by Hornsby *et al.* [27, 28], as also listed in Table 1. A concentric circular magnetic geometry is adopted, with temperature and density profiles, as shown in the top panel of Fig. 5. It is worth noting that the normalization differs between the two codes, such that $\rho_{\text{GENE}}^* = (\rho_{\text{GKW}}^*/\sqrt{2})(R/a)$. Moreover, it is important to highlight that the study by Hornsby *et al.* solely focuses on an electron current density and does not consider an ion current density. Hence we apply the same convention in GENE for this particular benchmark.

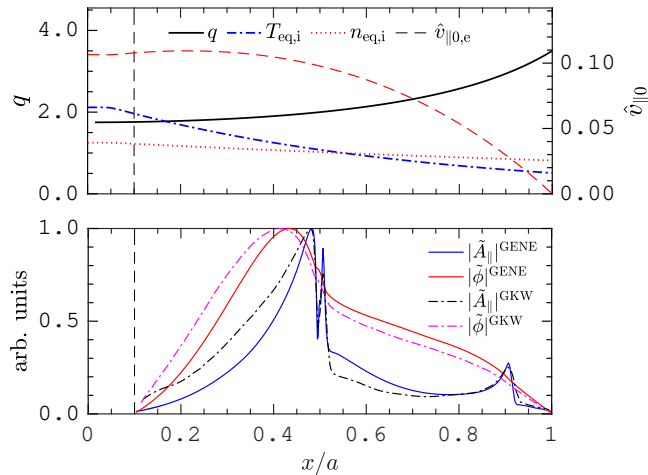


Figure 5. [Top] Equilibrium quantities used for the benchmark with GKW [27, 28] (case 3 in Table 2). Profiles of safety factor (black solid line), temperature (blue dash-dotted), and density (red dotted) are on the left axis, and velocity shift (red dashed) is referenced on the right axis. [Bottom] The corresponding normalized radial eigenmode structures obtained from GENE in comparison with GKW.

The radial tearing-mode structures obtained from GENE, depicted in the bottom panel of Fig. 5, match those from GKW. These mode structures exhibit a fundamental tearing feature, characterized by abrupt changes in radial mode structures at rational surfaces, i.e., $q = 2/1$ at $x/a = 0.5$ and $q = 3/1$ at $x/a = 0.9$. The ratio of the peaks of electrostatic to electromagnetic potentials, as determined by GENE, is comparable to the ratio reported in Ref. [28] for GKW. A comparison of growth rates and frequencies at different values of plasma β and pressure gradients, as presented in Table 2, demonstrates good agreement between the two codes. Slight deviations in Cases 4 and 5 can be attributed to small growth rates, as they fall within the range of computational error bars.

The comparison shows that GKW and GENE, though implemented slightly differently, agree on global-tearing growth rates and frequencies, even under the influence of diamagnetic effects, i.e., density and temperature gradients.

| Case | β_e (%) | R/L_n | R/L_T | GKW | | GENE | |
|------|---------------|---------|---------|-----------------------|-----------------------|-----------------------|-----------------------|
| | | | | $\gamma/[v_{Th}/R_0]$ | $\omega/[v_{Th}/R_0]$ | $\gamma/[v_{Th}/R_0]$ | $\omega/[v_{Th}/R_0]$ |
| 1 | 0.05 | 1.5 | 5.0 | 0.045 | -0.16 | 0.048 | -0.16 |
| 2 | 0.10 | 1.0 | 3.5 | 0.032 | -0.12 | 0.031 | -0.11 |
| 3 | 0.10 | 1.5 | 5.0 | 0.024 | -0.15 | 0.023 | -0.17 |
| 4 | 0.20 | 1.5 | 5.0 | 0.009 | -0.15 | 0.012 | -0.09 |
| 5 | 0.10 | 2.2 | 6.9 | 0.0032 | -0.28 | 0.0070 | -0.24 |

Table 2. Comparison of growth rates and frequencies between GKW and GENE at different plasma β s and gradients.

3.3. Comparison with Fluid Model

A resistive reduced two-fluid model has successfully described tearing modes and has been utilized to investigate the interactions between large-scale tearing modes and small-scale KBM [42]. It is useful to compare tearing modes modeled with the gyrokinetic model with those produced by the fluid model. Hence, we adopt the safety-factor and pressure profiles employed in Ref. [42] in this benchmark. These equilibrium profiles have been previously demonstrated to generate tearing modes for the investigation of thermal transport in the presence of magnetic fluctuations, as well as island formation and rotation [2].

Table 1 exhibits the analytical expressions of the safety factor, temperature, and density profiles. The safety factor at the magnetic axis is $q_0 = 1.7$, and the value at the minor radius is $q_a = 4.0$, as illustrated in the top panel of Fig. 6. The corresponding shifted velocity calculated from Eq. (16) is also shown. Notably, the q -profile exhibits resonance of the tearing mode at the $q = 2$ surface located at $r/a = 0.65$.

The tearing-mode's radial mode structure produced in GENE is shown in the bottom panel of Fig. 6, highlighting the characteristics of the $m/n = 2/1$ mode and the subdominant structure of the $m/n = 3/1$ mode. Fig. 7 shows the poloidal cross-section with a 2/1 island feature, closely matching the corresponding result shown in Ref. [42]. Figure 8 shows a collisionality scan that demonstrates destabilization of tearing modes by collisionality. The growth rate of the $n = 1$ mode scales as the theoretical prediction [40, 41]. The growth rate spectrum is shown in Fig. 9. Although the growth rate for each toroidal mode number n does not exactly trace the points obtained from the fluid model, they agree within the uncertainty implied by the scatter of the data points of the fluid model.

4. Tearing Modes in the MST-RFP

Verification of the modified global GENE code against various computational models, as demonstrated in the preceding section, indicates the capability to accurately reproduce linear tearing modes in the RFP. Furthermore, it provides confidence that the code will serve as a valuable tool for investigating the nonlinear evolution of tearing modes, TEMs,

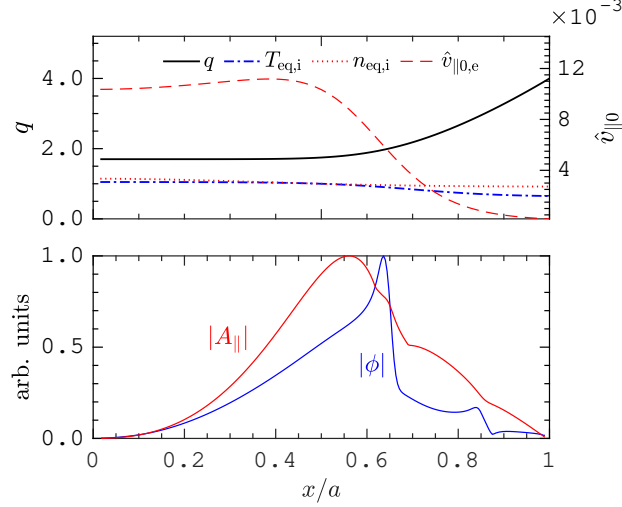


Figure 6. [Top] Equilibrium quantities used for the benchmark with a two-fluid model [42]. The left axis are profiles of safety factor (black solid), temperature (blue dash-dotted), and density (red dotted); on the right axis is the velocity shift (red dashed). [Bottom] The corresponding normalized radial eigenmode structures of the $n = 1$ tearing mode

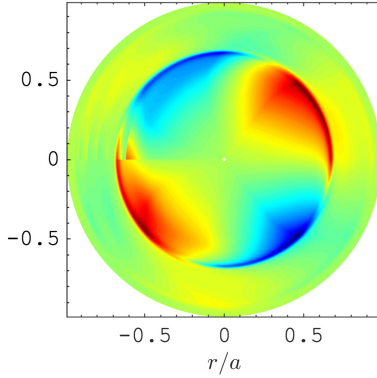


Figure 7. A poloidal cross-section of the electrostatic potential of the $n = 1$, $m = 2$ tearing mode obtained from GENE for the equilibrium used in the benchmark against the two-fluid model. This poloidal mode structure agrees with the corresponding structure shown in [42]

and multi-scale interactions within the RFP system. Analysis of multiscale interactions is a major undertaking and initial efforts will be presented in a separate paper. In this section, simulation of linear tearing modes for an RFP equilibrium will be shown and analyzed, followed by simulation of nonlinear tearing modes and their saturation.

RFPs are characterized by toroidal (B_{φ}) and poloidal (B_{θ}) magnetic-field components that are of comparable magnitude. As a result, the safety factor in RFPs is much lower than unity. Specifically, at the magnetic axis, the safety factor value is typically given by $q(x_a = 0) \sim a/(2R)$. As we move towards the plasma edge, the magnitude of the toroidal magnetic field gradually decreases, in standard RFP discharges

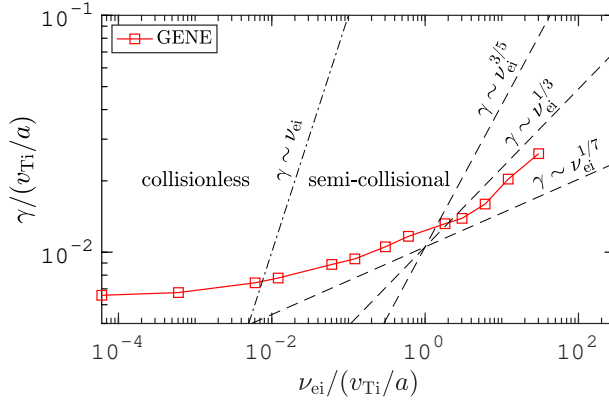


Figure 8. Growth rate of the $n = 1$ tearing mode as a function of the electron-ion collision frequency for a benchmarking case with the two-fluid model, showing destabilization of the tearing modes with collisionality, obeying a scaling that follows theoretical predictions [40, 41].

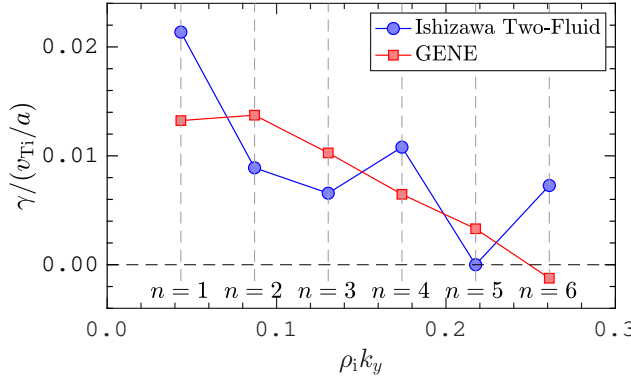


Figure 9. Growth rate spectrum of tearing mode obtained from GENE (blue circles) and the two-fluid model (red square).

eventually reversing its direction. Consequently, the safety factor q decreases with minor radius and becomes negative at the edge, which is in contrast to tokamaks where q increases toward the edge. Both the toroidal and poloidal magnetic-field components in RFPs vary strongly with minor radius, which leads to significant magnetic shear. Combined with the low value of q , this enables the formation of low-order rational surfaces, making the plasma vulnerable to tearing modes [9].

This study utilizes semi-analytical equilibrium profiles of the RFP obtained from the MSTFit reconstruction code [49], which solves the Grad-Shafranov equation using experimental data from the Madison Symmetric Torus (MST), discharge #1130819032. In Fig. 10a, the q -profile is presented for a discharge with the reversal surface located at the plasma edge. This non-reversed discharge is referred to as an $F = 0$ discharge, where F is the reversal parameter defined as $F = B_\varphi(a)/\langle B_\theta \rangle$. The choice of an $F = 0$ discharge is computationally favored for GENE since it avoids encountering the reversal

surface and $q = 0$. In $F = 0$ discharges, the specific nonlinear saturation mechanism for tearing modes has not been definitively identified, unlike reversed discharges where the turbulent cascade is known to be mediated by $m = 0$ modes resonant at the reversal surface [3].

The total current profile, shown in Fig. 10b, is utilized to calculate the shifted velocity (see Fig. 10e) for the shifted Maxwellian distribution function, as outlined in Eq. (12). To mitigate numerical instability near the edge, we introduce a flattened region in the shifted velocity. This adjustment is expected to have a negligible impact on the linear growth rates and structures of tearing modes. The same adjustment is applied to nonlinear simulations. It is important to note that the edge region displays significant density and temperature gradients, seen in Fig. 10c-d, which can give rise to microinstabilities, particularly the ∇n -driven TEM [19, 29].

The nominal plasma parameters are computed at the center of the computational domain, i.e., at $r/a = 0.45$. The reference β_e is found to be 0.69%. The normalized gyroradius ρ_i^* is calculated to be 1.46×10^{-2} . Since deuterium was used in the experimental setup of MST, the mass ratio employed in the simulation is $m_e/m_i = 2.73 \times 10^{-4}$. The electron temperature T_{0e} serves as a reference temperature, while T_{0i} is set at 40% of T_{0e} [7]. Considering collisions, the simulation incorporates the Landau collision operator with a collision frequency of $\nu_{ei} = 0.242 c_s/R_0$. Various other collision operators were tested and yielded comparable linear growth rates. To maintain numerical stability and prevent fluctuations near the boundaries, a Dirichlet boundary condition with the Krook damping operator is applied to the buffer zones, which occupy 5% of the radial domain on both ends. Heat and particle sources are applied in these zones to prevent the fluctuating quantities from deviating strongly from equilibrium, which can violate the δf approximation. The $n = 5$ resonant surface is close to the magnetic axis, so the simulation domain is positioned as close as feasible to the axis to mitigate mode suppression by the boundary. Accordingly, the simulation conducted is within the range $r/a = [0.005, 0.885]$. The resolution employed in this case involves grid point counts for radial and parallel displacements, and for the parallel velocity and magnetic moment, with values of $N_x = 512$, $N_z = 16$, $N_{v\parallel} = 32$, and $N_\mu = 16$, respectively.

In light of the distinct magnetic geometry of the RFP compared to that of the tokamak, the standard concentric circular magnetic geometry often used in GENE is ill-suited for accurately representing its true geometry. To overcome this constraint, Carmody et al. [29] proposed an alternative circular geometry that accounts for the specific characteristics of RFPs. This modified approach, known as adjusted circular geometry, employs circular flux surface cross sections while incorporating a polynomial fit factor $f(r/R_0)$ to precisely capture the spatial variations of the total magnetic field across the radial extent. Specifically,

$$\mathbf{B} = \frac{R_0 B_0}{R} |q| f(r/R_0) \left(\mathbf{e}_\phi + \mathbf{e}_\theta \frac{r}{R_0 \bar{q}} \right), \quad (20)$$

where R_0 and r are the major and minor radii at the axis and of the flux surface,

respectively, $R = R_0 + r \cos \theta$, while B_0 is the total background magnetic field on the axis, and θ is the poloidal angle. The safety factor at the center of the simulation domain is denoted as q , and $\bar{q} = q\sqrt{1 - (r/R_0)^2}$. The polynomial fit $f(r/R_0)$ allows consistency for the toroidal field when r approaches the edge of the plasma. The model has been benchmarked and validated in studying microturbulence in the RFP [29], and we modified and implemented this geometry for global simulations.

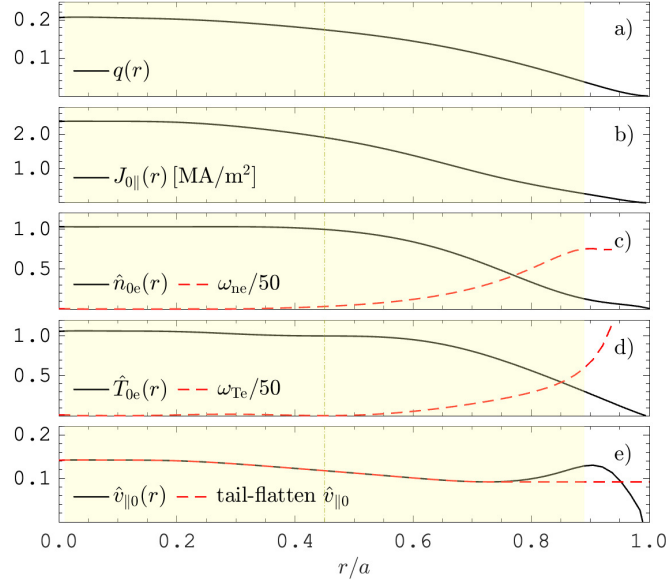


Figure 10. Equilibrium profiles of an $F = 0$ discharge obtained from the MSTFit reconstruction code. The simulation domain is in the yellow area $r_a = [0.005, 0.895]$ with the center at $r_a = 0.45$.

4.1. Linear Analysis

Since the q -profile on the axis has a maximum value slightly above 0.2, this allows the lowest possible resonating $(m, n) = (1, 5)$ tearing mode to occur at $q = 0.2$. Linear simulations performed with $n \geq 5$ are shown in Fig. 11, illustrating the radial structures of the electrostatic potential ϕ and the electromagnetic parallel vector potential A_{\parallel} of the $n = 5$ and $n = 6$ modes, along with some of their corresponding higher harmonics. Mode structures extend throughout the radial domain and exhibit well-known characteristics similar to those found in the benchmarking cases, i.e., an abrupt change in ϕ and A_{\parallel} at the rational surfaces. The poloidal cross-section of the electrostatic potential of the $n = 5$ and $n = 6$ modes is illustrated in Fig. 12, clearly exhibiting the presence of an $m = 1$ island, which is indicative of a tearing mode.

Figure 13 shows the linear spectrum for different values of n . Among these modes, the ones with $n = 5$ and $n = 6$ exhibit linear instability, as they are directly driven by gradients in the background current. On the other hand, the mode with $n = 7$ is marginally stable. Higher-order modes that are not resonant with $n = 5$ and $n = 6$, e.g.,

$n = 8, 9, \dots$, are found to be stable. Linear simulation in GENE allows for a single n value but encompasses all attainable m modes at different rational surfaces. For $n = 5$, only the $m = 1$ resonant surface lines within the simulation domain, while for $n = 10$, two m modes can be resonance: $m = 1$, which resonates near $r_a = 0.74$, and $m = 2$, which coincides with the resonance location of $(m, n) = (1, 5)$, see Fig. 11.

The spectrum in Fig. 13 indicates that the growth rates of the dominant n modes are approximately three orders of magnitude smaller than the Alfvén frequency γ_A . This observation reflects the characteristic behavior of tearing modes, which exhibit significantly slower growth than an inverse Alfvén time. Additionally, our analysis reveals that the fundamental mode frequencies fall within the range of frequencies obtained from the MST experiment, specifically around 5-25 kHz [16, 50]. This correspondence suggests that the tearing modes generated in our simulation are consistent with those observed in the experimental setting.

As n , and correspondingly k_y , increases, the growth rates gradually diminish, eventually stabilizing at approximately $k_y = 0.15$. For $n \geq 35$, the instabilities exhibit more electrostatic behavior, with $|\phi|/|A_{\parallel}| > 10$, with the mode peak localized near the plasma edge. These particular instabilities are identified as ∇n -TEM and will be the subject of comprehensive discussion in a separate publication.

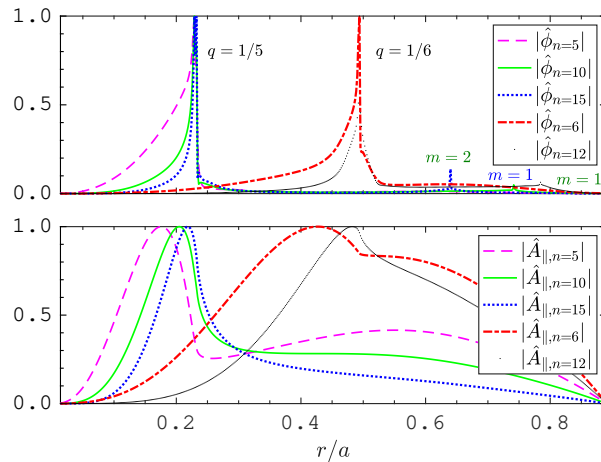


Figure 11. Radial mode structures of linear tearing modes. [Top] Electrostatic potential structures and [bottom] electromagnetic potential structures. Different n modes can resonant at the same rational surface, but with different multihelicities m .

Consistent with the benchmark cases, the collisionality scans with $n = 5$ and $n = 6$ show destabilization at larger collision frequencies, indicating tearing instability for the RFP equilibrium. Figure 14 shows the collisionality scan and indicates that there are collisionless and semi-collisional regimes at lower and higher collisionalities, respectively. The mode with $n = 5$ shows a scaling $\gamma \propto \nu_{ei}^{1/7}$, while the $n = 6$ mode scales as $\gamma \propto \nu_{ei}^{1/3}$ in the semi-collisional regime.

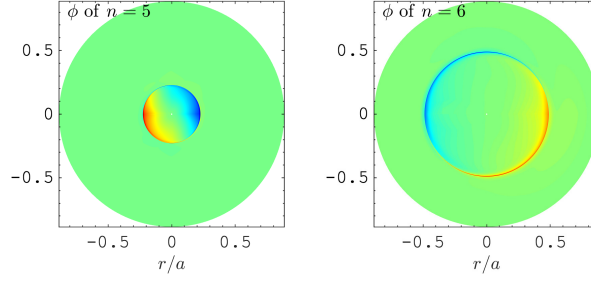


Figure 12. Poloidal cross-section of $n = 5$ [left] and $n = 6$ [right] electrostatic potential showing $m = 1$ eigenmode structure on the $q = 0.2$ and $q = 0.16$ rational surfaces, respectively.

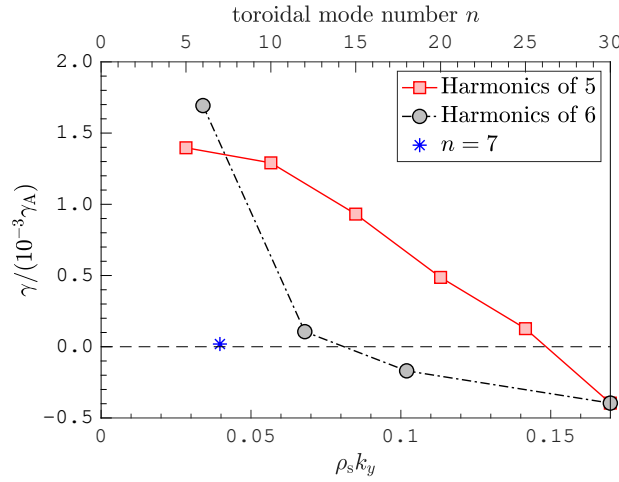


Figure 13. Linear tearing mode spectrum with respect to toroidal wavenumber. Note that $\gamma_A = B_0/\sqrt{4\pi n_e m_i}/L_s$ and L_s is the magnetic shear length defined as $L_s = r_s/\hat{s} = (r_s/R)(1/q'(r_s))$ with r_s the plasma radius at the rational surface of interest.

4.2. Nonlinear Evolution

Nonlinear simulations of a single-scale tearing mode are performed including with $n = 0, 6, 12$, and 18 . The nonlinear simulation otherwise employs the same resolutions as those used in the converged linear calculations. Figure 15 illustrates mode evolution in the simulation, showing an extended transient phase lasting approximately 70% of the total simulation time before reaching nonlinear saturation.

The growth of the unstable mode with $n = 6$ is initially slow and continues until the time $t = 1300 R_0/c_s$. During this early stage, the simulation reveals no significant interactions among modes, as evident in the second row of Fig. 15. The current density fluctuation confirms the initial presence of a single tearing mode resonating at a rational surface with $q = 1/6$. This mode exhibits approximately linear growth, and there is no clear coupling observed with other modes. However, once the fastest-growing mode reaches a certain amplitude, it starts to couple with the linearly stable mode resonating

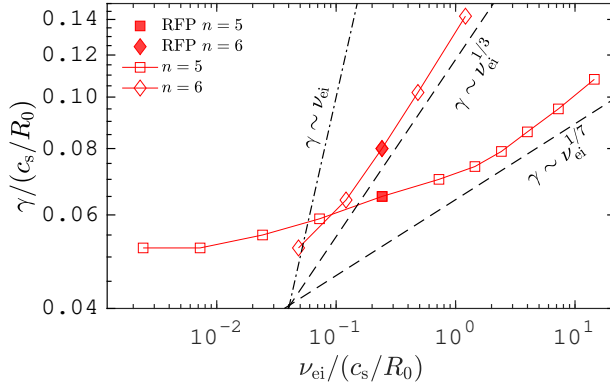


Figure 14. Collisionality scan for the $n = 5$ tearing modes, showing two collisionality regimes: a collisionless regime where the growth rate asymptotically approaches a constant at very low collisionality, and a semi-collisional regime where the growth rates increase with a scaling of $\nu_{\text{ei}}^{1/7}$. Semi-collisional regime of $n = 6$ is also plotted, showing scaling of $\nu_{\text{ei}}^{1/3}$. A solid square and a solid diamond mark the growth rates of $n = 5$ and $n = 6$, respectively, at the collisionality representing MST-RFP, evaluated from given equilibria.

at $q = 1/9$. In this simulation, this corresponds to mode $m = 2$, $n = 18$, as the mode with $n = 9$ is not present in the simulation. The coupling occurs between mode $m = 2$ and mode $m = 1$, with energy being transferred from mode $m = 1$ to mode $m = 2$. This energy transfer is observed as the onset of oscillations around $t \approx 1850$. As the coupling involves a third mode with $(m, n) = (1, 12)$, the fluctuations become more irregular. The interaction among all three modes leads to the saturation phase, where the fluctuation reaches a quasi-steady state. By $t = 2080$, the tearing modes are fully nonlinearly coupled, resulting in a stronger and higher peak in mode $m = 1$, $n = 12$. It is important to note that the $m = 0$ mode does not play a significant role in energy mediation, unlike the reversed discharges studied in Ref. [3]. In the present case, the $m = 0$ mode is non-resonant and does not exhibit noticeable coupling with other modes in the system.

5. Conclusions

Tearing-mode fluctuations are significant players in the dynamics of RFP plasmas. It had been established from nonlinear simulations of ∇n -TEM turbulence with the inclusion of an external magnetic field to model tearing modes, that tearing modes erode the microturbulent zonal flows and enhance the nonlinear electrostatic heat flux. Further studies of the interaction of slab ITG instability with a local code utilizing a shifted Maxwellian in the perturbed distribution had also indicated an effect of the tearing modes on the ITG turbulence level. However, these studies did not realistically model global tearing modes, with a lack of curvature effects, and did not account for the equilibrium current. The work described here is a modification of the global

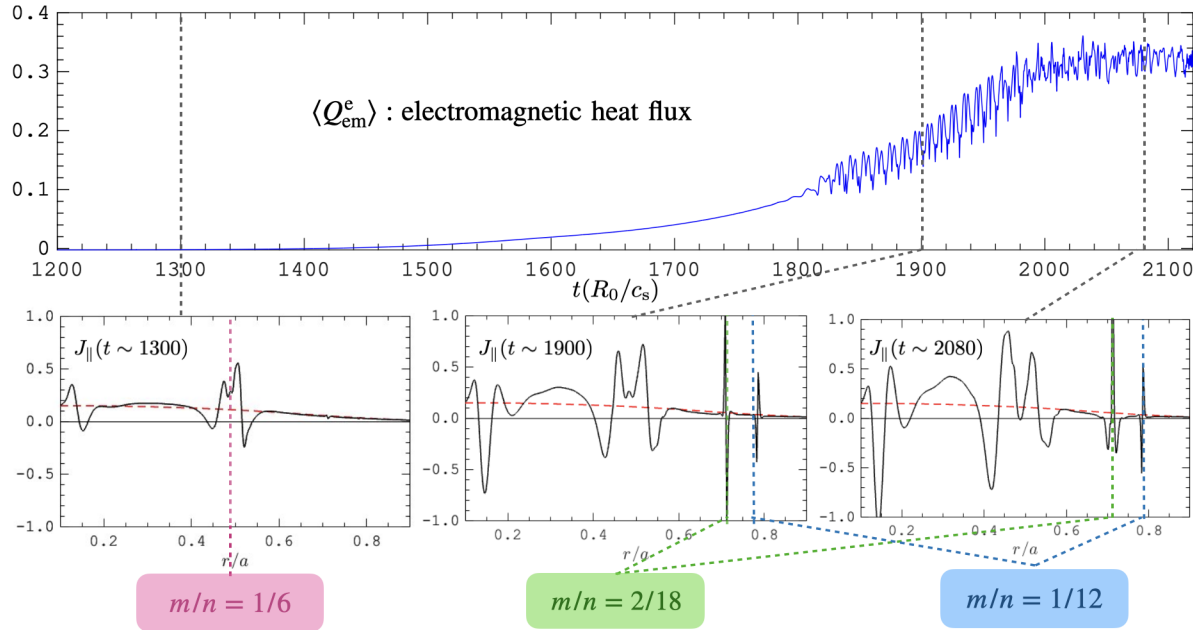


Figure 15. [Top] Time history of electromagnetic electron heat flux, and [bottom] radial profiles of fluctuating parallel velocity representing the parallel current density at different time snapshots. At $t \approx 1300$, only the strongest growing mode $m = 1, n = 6$ leads to a significant fluctuation level at the single rational surface. At $t \approx 1900$, modes $m = 1$ and $m = 2$ start to couple and lead to oscillation of the heat flux. At $t \approx 2080$, energy is transferred to $m = 1, n = 12$, as mediated by the $m = 2$ mode. Fluctuations are more irregular at this stage. The $m = 1, n = 12$ mode grows faster with a larger amplitude. Once the modes reach a quasi-stationary state, energy injected by the instability is balanced by dissipation at smaller scales.

gyrokinetic code GENE to include current-gradient-drive terms arising from a shifted Maxwellian in the equilibrium distribution function. Implementation of the shifted Maxwellian distribution in the gyrokinetic equations enables realistic calculations of toroidal tearing mode instability and its nonlinear evolution self-consistently. The implementation includes modifying field equations and higher velocity moments to obtain physical observables under the shifted Maxwellian.

The modified GENE code was benchmarked against different computational models. Comparisons were performed with the gyrokinetic PIC full- f code ORB5, the δf continuum code GKW, a reduced fluid model, and analytic theory. In comparison with the discrete gyrokinetic PIC code ORB5 utilizing gyrokinetic ions and electrons, scans over electron plasma β and mass ratios show agreement between the two codes and consistency with theoretical scaling. A similar comparison was done using the equilibrium from Ref. [28], where simulations of a linear tearing mode calculation using a continuous gyrokinetic code GKW. The growth rates obtained from GENE with different pressure gradients match well with results from GKW. Radial mode structures of the electrostatic and electromagnetic potentials and their peak ratios also match well. When the equilibria from the fluid simulation of Ref. [42] were introduced for further testing,

the modified GENE code produced mode structures that are in good agreement with the mode structures of the fluid calculation. The collisionality scaling and growth rate spectrum additionally confirm the characteristics of global tearing modes. This establishes that the modified GENE code captures global tearing-mode dynamics, and is well equipped to study global tearing modes driven by the background current density in the RFP. While there exists a substantial body of research concerning benchmarking of microinstabilities in gyrokinetic codes, and MHD-scale instabilities in MHD codes, code-code comparisons using gyrokinetic simulations for MHD-scale modes have remained relatively limited. The present study represents results addressing this gap.

Having performed this verification work, the code was then utilized to study the linear stability of a non-reversed $F = 0$ discharge in MST. With the equilibrium modeled by the adjusted circular magnetic geometry of GENE, the simulation found that the most unstable linear tearing modes are $n = 5$, which is close to the magnetic axis, and $n = 6$, which is near the middle of the domain. Modes with $n = 10$ and $n = 12$ are also unstable. Higher harmonics eventually become stable, consistent with the stabilizing effect of larger k_y . Radial mode structures and collisionality scans confirm that the global instability observed in MST geometry is indeed a tearing instability.

A nonlinear tearing mode simulation was also performed, treating the nonlinear interaction of multiples of $n = 6$ modes. The nonlinear simulation reaches saturation by excitation and coupling of modes at different n numbers, mediated by interaction with the $m = 2$ mode, instead of the $m = 0$ mediator commonly seen in simulations of reversed discharges. The mode coupling transfers energy to higher n , consistent with the well-known magnetic energy cascade in the RFP.

The results from nonlinear simulations provide an illustration of how large-scale tearing modes, active in the core, excite tearing modes at outer radii and thus potentially influence the small-scale TEMs near the edge. Namely, through mode coupling mediated by the $m = 2$ component, low-order- n modes couple and transfer energy to higher- n , stable tearing modes. The coupling and cascading continue through multiple stages, leading to the spreading of energy towards finer-scale tearing modes at higher n , and progressing towards the edge. As a result, this progression leads to the excitation of stable tearing modes near the plasma edge, demonstrating the capability of exerting an influence on the TEM region of MST.

This study of self-consistent linear and nonlinear tearing modes in the RFP lays the foundation for the investigation of multi-scale interactions with microturbulent fluctuations, which will be carried out in future work. Ongoing investigations of multi-scale interactions in the RFP, which will be reported separately, will inform both the magnetic turbulence properties of the RFP and interactions of magnetic perturbations with microturbulence in tokamak systems.

Acknowledgement

The authors express sincere gratitude to J. K. Anderson for providing the $F = 0$ equilibrium profiles obtained from the MSTFit reconstruction code. Additionally, the authors extend their appreciation to C. R. Sovinec for the valuable discussions regarding the numerical simulation of global tearing modes in the RFP. Special thanks are also due to Z. R. Williams and the developers of the GENE code for offering assistance in implementing the global code for our study.

References

- [1] W.A. Hornsby, P. Migliano, R. Buchholz, D. Zarzoso, F.J. Casson, E. Poli, and A.G. Peeters, *Plasma Phys. Control. Fusion* **53**, 054008 (2015)
- [2] A. Ishizawa, Y. Kishimoto, and Y. Nakamura, *Plasma Phys. Control. Fusion* **61**, 054006 (2019)
- [3] Y.L. Ho and G.G. Craddock, *Phys. Fluids B: Plasma Phys.* **3**, 721 (1991)
- [4] J.S. Sarff, S.A. Hokin, H. Ji, S.C. Prager, and C.R. Sovinec, *Phys. Rev. Lett.* **72**, 3670 (1994)
- [5] B.E. Chapman, A.F. Almagri, M. Cekic, D.J. Den Hartog, S.C. Prager, and J.S. Sarff, *Phys. Plasmas* **3**, 709 (1996)
- [6] B.E. Chapman, “*Fluctuation reduction and enhanced confinement in the MST reversed-field pinch*,” Ph.D. Thesis (The University of Wisconsin-Madison, 1997)
- [7] B.E. Chapman, A.F. Almagri, J.K. Anderson, T.M. Biewer *et al.*, *Phys. Plasmas* **9**, 2061 (2002)
- [8] B.E. Chapman, J.W. Ahn, A.F. Almagri, J.K. Anderson *et al.*, *Nucl. Fusion* **49**, 104020 (2009)
- [9] L. Marrelli, P. Martin, M.E. Puiatti, J.S. Sarff, B.E. Chapman, J.R. Drake, D.F. Escande, and S. Masamune, *Nucl. Fusion* **61**, 023001 (2021)
- [10] S. Hokin, A. Almagri, S. Assadi, J. Beckstead *et al.*, *Phys. Fluids B: Plasma Phys.* **3**, 2241 (1991)
- [11] G. Fiksel, S.C. Prager, W. Shen, and M.R. Stoneking, *Phys. Rev. Lett.* **72**, 1028 (1994)
- [12] F. Ebrahimi, V.V. Mirnov, S.C. Prager, and C.R. Sovinec, *Phys. Rev. Lett.* **99**, 075003 (2007)
- [13] D.F. Escande, P. Martin, S. Ortolani, A. Buffa *et al.*, *Phys. Rev. Lett.* **85**, 1662 (2000)
- [14] P. Martin, L. Marrelli, G. Spizzo, P. Franz *et al.*, *Nucl. Fusion* **43**, 1855 (2003)
- [15] R. Lorenzini, E. Martines, P. Piovesan, D. Terranova *et al.*, *Nature Phys.* **5**, 570 (2009)
- [16] Y. Ren, A.F. Almagri, G. Fiksel, S.C. Prager, J.S. Sarff, and P.W. Terry, *Phys. Rev. Lett.* **107**, 195002 (2011)
- [17] D.J. Thuecks, A.F. Almagri, J.S. Sarff, and P.W. Terry, *Phys. Plasmas* **24**, 022309 (2017)
- [18] J.B. Titus, A.F. Almagri, P.W. Terry, J.S. Sarff, E.D. Mezonlin, and J.A. Johnson III, *Phys. Plasmas* **28**, 062504 (2021)
- [19] Z.R. Williams, M.J. Pueschel, P.W. Terry, and T. Hauff, *Phys. Plasmas* **24**, 122309 (2017)
- [20] T.E. Evans, M.E. Fenstermacher, R.A. Moyer, T.H. Osborne *et al.*, *Nucl. Fusion* **48**, 024002 (2008)
- [21] G.R. McKee, Z. Yan, C. Holland, R.J. Buttery, T.E. Evans, R.A. Moyer, S. Mordijk, R. Nazikian, T.L. Rhodes, O. Schmitz, and M.R. Wade, *Nucl. Fusion* **53**, 113011 (2013)
- [22] Z.R. Williams, M.J. Pueschel, P.W. Terry, T. Nishizawa, D.M. Kriete, M.D. Nornberg, J.S. Sarff, G.R. McKee, D.M. Orlov, and S.H. Nogami, *Nucl. Fusion* **60**, 096004 (2020)
- [23] M.J. Pueschel, D.R. Hatch, M. Kotschenreuther, A. Ishizawa, G. Merlo, *Nucl. Fusion* **60**, 124005 (2020)
- [24] A.J. Brizard and T.S. Hahm, *Rev. Mod. Phys.* **79**, 421 (2007)
- [25] D. Liu, W. Zhang, J. McClenaghan, J. Wang, and Z. Lin, *Phys. Plasmas* **21**, 122520 (2014)
- [26] D. Liu, J. Bao, T. Han, J. Wang, and Z. Lin, *Phys. Plasmas* **23**, 022502 (2016)
- [27] W.A. Hornsby, P. Migliano, R. Buchholz, L. Kroenert, A. Weikl, A.G. Peeters, D. Zarzoso, E. Poli, and F.J. Casson, *Phys. Plasmas* **22**, 022118 (2015)
- [28] W.A. Hornsby, P. Migliano, R. Buchholz, S. Grosshauser, A. Weikl, D. Zarzoso, F.J. Casson, E. Poli, and A.G. Peeters, *Plasma Phys. Control. Fusion* **58**, 014028 (2015)

- [29] D. Carmody, M.J. Pueschel, J.K. Anderson, and P.W. Terry, *Phys. Plasmas* **22**, 012504 (2015)
- [30] Z.R. Williams, “*On the Interactions of Magnetic Fluctuations, Zonal Flows, and Microturbulence in Fusion Plasmas*,” Ph.D. Thesis (The University of Wisconsin-Madison, 2019)
- [31] F. Jenko, W. Dorland, M. Kotschenreuther, and B.N. Rogers, *Phys. Plasmas* **7**, 1904 (2000)
- [32] T. Görler, N. Tronko, W.A. Hornsby, A. Bottino, R. Kleiber, C. Norscini, V. Grandgirard, F. Jenko, and E. Sonnendrücker, *Phys. Plasmas* **23**, 072503 (2016)
- [33] A. Di Siena, T. Görler, H. Doerk, R. Bilato, J. Citrin, T. Johnson, M. Schneider, E. Poli, and JET Contributors, *Phys. Plasmas* **25**, 042304 (2018)
- [34] A. Di Siena, “*Implementation and investigation of the impact of different background distributions in gyrokinetic plasma turbulence studies*,” Ph.D. Thesis (Ulm University, 2019)
- [35] <https://genecode.org>
- [36] S. Jolliet, A. Bottino, P. Angelino, R. Hatzky, T.M. Tran, B.F. Mcmillan, O. Sauter, K. Appert, Y. Idomura, and L. Villard, *Comput. Phys. Commun.* **177**, 409 (2007)
- [37] D.R. Ernst, J. Lang, W.M. Nevins, M. Hoffman, Y. Chen, W. Dorland, and S. Parker, *Phys. Plasmas* **16**, 055906 (2009)
- [38] A. Di Siena, A. Biancalani, T. Görler, H. Doerk, I. Novikau, P. Lauber, A. Bottino, E. Poli, and The ASDEX Upgrade Team, *Nucl. Fusion* **58**, 106014 (2018)
- [39] H.P. Furth, J. Killeen, and M.N. Rosenbluth, *Phys. Fluids* **6**, 459 (1963)
- [40] J.F. Drake and Y.C. Lee, *Phys. Fluids* **20**, 1341 (1997)
- [41] F. Porcelli, *Phys. Rev. Lett.* **66**, 425 (1991)
- [42] A. Ishizawa and N. Nakajima, *Nucl. Fusion* **49**, 055015 (2009).
- [43] T. Görler, X. Lapillonne, S. Brunner, T. Dannert, F. Jenko, F. Merz, and D. Told, *J. Comput. Phys.* **230**, 7053 (2011)
- [44] M.J. Pueschel, T. Dannert, and F. Jenko, *Comput. Phys. Commun.* **181**, 1428 (2010)
- [45] A. Biancalani, A. Bottino, C. Ehrlacher, V. Grandgirard *et al.*, *Phys. Plasmas* **24**, 062512 (2017)
- [46] A. Di Siena, T. Görler, E. Poli, A. Bañón Navarro, A. Biancalani, R. Bilato, N. Bonanomi, I. Novikau, F. Vannini, and F. Jenko, *J. Plasma Phys.* **87**, 555870201 (2021)
- [47] A.G. Peeters, Yann Camenen, F. James Casson, W.A. Hornsby, A.P. Snodin, D. Strintzi, and Gabor Szepesi *Comput. Phys. Commun.* **180**, 2650 (2009)
- [48] J.P.M. Collar, B.F. McMillan, S. Saarelma, and A. Bottino, *Plasma Phys. Control. Fusion* **62**, 095005 (2020)
- [49] J.K. Anderson, C.B. Forest, T.M. Biewer, J.S. Sarff, and J.C. Wright *Nucl. Fusion* **44**, 162 (2003)
- [50] J.S. Sarff, S. Assadi, A.F. Almagri, M. Cekic *et al.*, *Phys. Fluids B: Plasma Phys.* **5**, 2540 (1993)